Earth and Planetary Science Letters 544 (2020) 116375

Contents lists available at ScienceDirect

Earth and Planetary Science Letters

www.elsevier.com/locate/epsl

Tibetan dichotomy exposed in the Canadian Shield: A lower crustal perspective

Gregory Dumond

Department of Geosciences, University of Arkansas, Fayetteville, AR 72701, USA

ARTICLE INFO

Article history:
Received 2 January 2020
Received in revised form 17 May 2020
Accepted 26 May 2020
Available online xxxx
Editor: R. Bendick

Keywords:
Canadian Shield
Tibetan Plateau
granulite
monazite
continental crust
shear zone

ABSTRACT

It has been hypothesized that much of central and eastern Tibet coincides with gravitationally driven flow of weak lower continental crust. Magnetotelluric profiles throughout Tibet reveal several deep crustal zones of high conductivity inferred to represent either melt-weakened channelized flow of deep crust or alternatively, migration of fluids or melts along shear zone-fault systems. In eastern Tibet, some workers suggest that deep crustal flow is diverted around cratonic lithosphere beneath the Sichuan basin. This behavior requires a weak versus strong rheological dichotomy in the lower crust. Evidence for this behavior is presented from a deeply exhumed granulite terrane (>0.6–1.6 GPa) in the western Canadian Shield. Data support the hypothesis that at 1.95–1.90 Ga, lower crust northwest of the >400 km-long Grease River shear zone was melt-weakened while lower crust southeast of the Grease River shear zone was dehydrated and strong. Strain localization and dextral transpressive shearing occurred at 1.91–1.90 Ga along the Grease River shear zone – the locus of a rheological dichotomy that represents a field-based analog for lower crust beneath the eastern Tibetan plateau. This work demonstrates that rheology of the lower continental crust can be spatially heterogeneous at <1 m^2 to 100s of km^2 scales. Deep crustal rheology also depends on fertility: melt weakening and flow during fluid-absent melting (>750 °C) and granulite-grade metamorphism is favored in "first-cycle" metasedimentary biotite-rich protoliths, though melt extraction can decrease this fertility. Older and previously dehydrated poly-metamorphic granulites tend to be stronger and less prone to pervasive lower crustal flow.

1. Introduction

The rheological behavior of Tibetan lower continental crust remains the subject of intense debate. Some workers maintain that the lower crust of Tibet is strong and mechanically coupled to the upper crust. Evidence for this strong behavior comes from numerical experiments, estimates of flexural rigidity of the lithosphere, and balanced cross-sections, among other data (Copley et al., 2011; Fielding and McKenzie, 2012; Lease et al., 2012). Other workers hypothesize that Tibetan lower crust is the site of low viscosity ductile flow that is decoupled from the upper crust (Royden et al., 2008). Evidence cited for weak lower crust beneath Tibet includes geophysically imaged zones of low shear wave velocity (Yao et al., 2010), high conductivity (Rippe and Unsworth, 2010), and sub-horizontal seismic reflectivity (Ross et al., 2004).

Our understanding of the rheological behavior of lower continental crust is strongly influenced by data collected remotely at the surface. These include topography (Clark and Royden, 2000), magnetotelluric observations (Bai et al., 2010), xenoliths (Hacker et al., 2000), and earthquakes (Andronicos et al., 2007), among other constraints. Additional data come from studies of exhumed lower continental crust (e.g. Percival et al., 1992). These rare deep crustal sections provide important field-based constraints that may be used as analogs for understanding modern orogenic systems.

This contribution explores evidence for melt weakening adjacent to strong lower crust that is preserved in a deep crustal granulite terrane in the western Canadian Shield (Fig. 1A). The boundary separating weak and strong crust coincides with a major intracontinental shear zone. Field mapping, geochemistry, phase equilibria modeling, and in situ monazite petrochronology were carried out to evaluate the style of deformation and contemporaneity of melting across a ~100 km^2 restored section of the terrane (along A–A′ in Fig. 1C). The new results fill a crucial gap in data within the terrane and, in combination with existing data, support the occurrence of a rheological dichotomy that is analogous to lower crustal flow inferred near eastern Tibet adjacent to strong lithosphere beneath the Sichuan basin (#1 in Fig. 1B; Clark et al., 2005).

E-mail address: gdumond@uark.edu.

https://doi.org/10.1016/j.epsl.2020.116375

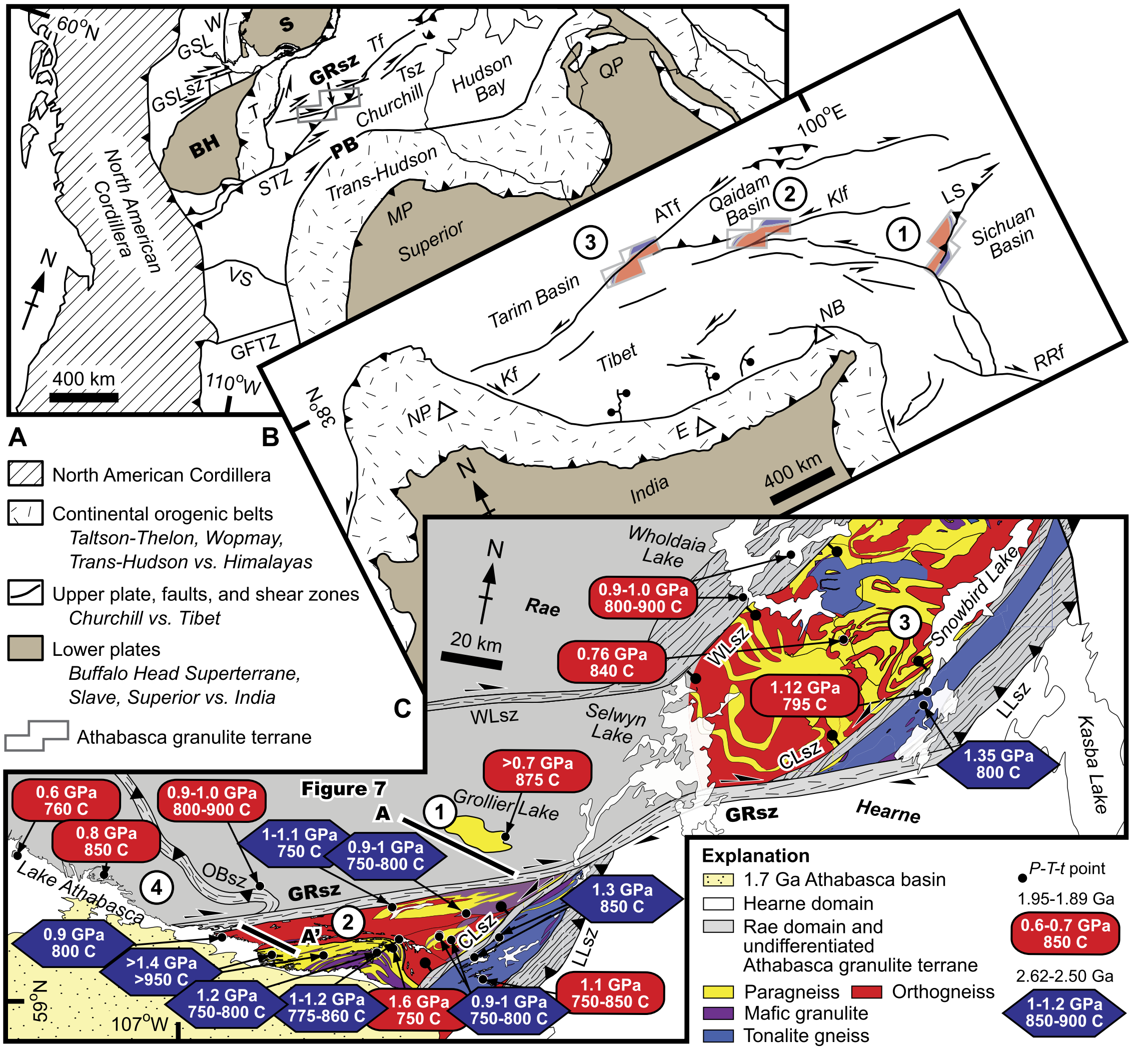

Fig. 1. Tectonic and geologic maps of North America, the Himalayan-Tibetan orogen, and the Athabasca granulite terrane. Figs. 1A and 1B are illustrated at the same scale and adapted from St-Onge et al. (2006). **A)** Tectonic map of the western Canadian Shield illustrating the upper plate Churchill Province and the lower plate domains that collided with it at 2.02–1.77 Ga – the Slave Province (S), Buffalo Head Superterrane (BH), and the Superior Province. Other abbreviations are: PB = Porter Bay arc; W = Wopmay orogen; GSL = Great Slave Lake; GSLsz = Great Slave Lake shear zone; T = Taltson-Thelon orogen; GRsz = Grease River shear zone; Tf = Tulemalu fault; Tsz = Tyrrell shear zone; STZ = Snowbird tectonic zone; VS = Vulcan structure; GFTZ = Great Falls tectonic zone; MP = Manitoba promontory; QP = Quebec promontory. **B)** Tectonic map of the Himalayan-Tibetan orogen adapted from Taylor and Yin (2009). Circled numbers 1, 2, and 3 are regions in Tibet discussed in the text where the Athabasca granulite terrane is proposed as an analogy for rheological dichotomies inferred near: 1 = Longmenshan fault system (Clark et al., 2005; Royden et al., 2008); 2 = Kunlun fault system (Le Pape et al., 2015); 3 = Altyn Tagh fault (Zhang et al., 2015). Abbreviations are: NP = Nanga Parbat; E = Everest; NB = Namche Barwa; Kf = Karakoram fault; ATf = Altyn-Tagh fault; Klf = Kunlun fault; LS = Longmenshan fault system; RRf = Red River fault. **C)** Geologic map of the Athabasca granulite terrane modified from Dumond et al. (2018). Circled numbers correspond to regions discussed in the text: 1 = Grollier Lake area (Knox et al., 2011; Ashton et al., 2017; this study); 2 = Mary batholith (Dumond et al., 2010); 3 = Snowbird Lake domain (Martel et al., 2008); 4 = Beaverlodge domain (Bethune et al., 2013). Note locations of the Grease River shear zone (GRsz) and *Pressure-Temperature*-time (*P-T*-t) data. Blue *P-T* points represent regions of Neoarchean high pressure metamorphism and melting that subsequently experienced protracted isobaric cooling. Red *P-T* points are high temperature domains that experienced partial melting +/− decompression in the Paleoproterozoic. Restoration of ∼110 km of strike-slip along the GRsz results in the Grollier Lake area occurring along strike of the Mary batholith using the reconstruction of Mahan and Williams (2005; line of section A–A′ in Fig. 1C).

2. Background

The >20,000 km^2 Athabasca granulite terrane in the western Canadian Shield of North America is one of Earth's largest exposures of lower continental crust. The Archean-Paleoproterozoic terrane consists of medium to high pressure felsic and mafic granulites and rare eclogite that equilibrated at >0.6 to 1.6 GPa (>20–60 km-depths; Fig. 1C; Dumond et al., 2018). The Grease River shear zone (GRsz) is a steeply NW-dipping, ∼7 km-wide, >400 km-long structure that cuts the Athabasca granulite terrane with at least 110 km of syn- to post-1.9 Ga dextral strike-slip offset (Figs. 1A and 1C; Mahan and Williams, 2005). Restoration of this offset results in the juxtaposition of the Grollier Lake area adjacent to the Mary batholith at 59°15' N, the latitude of Lake Athabasca (#1–2 and line of section A–A′ in Figs. 1C and 8A; Mahan and Williams, 2005). This restored transect is the focus of this study. Quartzo-feldspathic granulite gneisses are the most common rock type along this transect. Existing pressure-temperature (*P-T*) conditions in wall rocks on either side of the shear zone range from >0.7–1.1 GPa and 750–900 °C (Fig. 1C; Dumond et al., 2018).

On the southeast side of the transect, Neoarchean top-to-the-SE flow of weak lower crust (manifested as sub-horizontal fabrics at 2.60–2.55 Ga) and felsic granulite dehydration in the Mary batholith exposed southeast of the GRsz was followed by >650 m.y. of near-isobaric cooling and development of strong cratonic continental lithosphere (#2 in Fig. 1C, Figs. 2A–B; Flowers et al., 2008; Dumond et al., 2010). Overprinting 1.92–1.89 Ga structures include m-scale dextral shear zones with steeply NW-dipping fo-

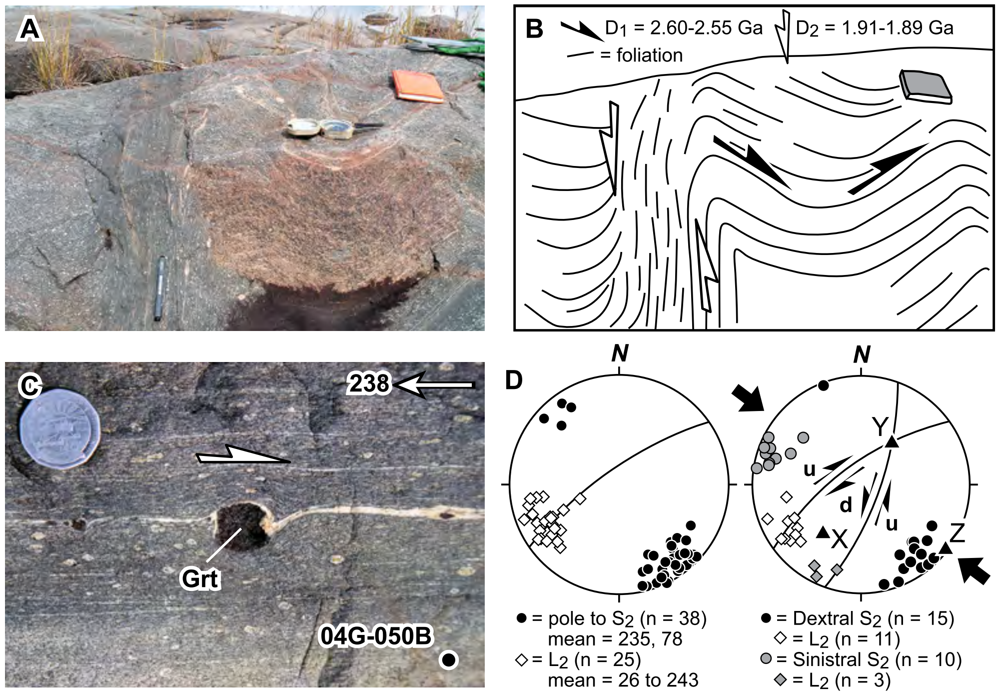

Fig. 2. Summary of field observations in the Mary batholith. **A-B)** Neoarchean sub-horizontal gneissic fabrics transposed by a Paleoproterozoic m-scale mylonitic sinistral shear zone (Dumond et al., 2010). **C)** Dextral mylonitic shear zone in the Mary batholith. Note location of sample 04G-050B dated in Figs. 7C and 7F. **D)** Stereonets illustrating Paleoproterozoic structures in the Mary batholith, including the predominant dextral, top-to-the-NE zones (left) and the record of finite strain (right) that results from treating the dextral and sinistral high strain zones as a conjugate pair, yielding NW-to-SE sub-horizontal contraction (Dumond et al., 2010).

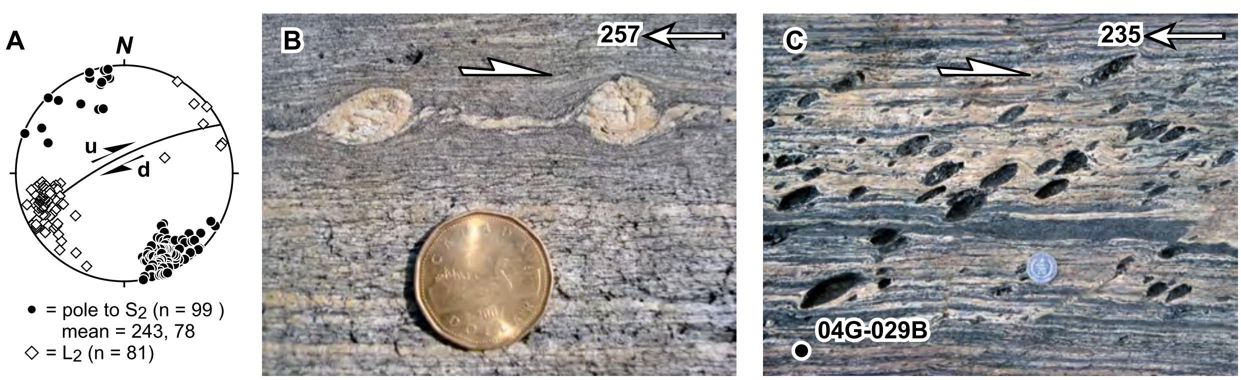

Fig. 3. Summary of field observations from the Grease River shear zone adjacent to the western margin of the Mary batholith (near #2 in Fig. 1C). **A)** Stereonet depicting structures mapped in Grease Bay by Dumond et al. (2010) indicating dextral top-to-the-NE transpressive shear strain. **B)** Dextral δ-porphyroclasts defined by K-feldspar in an orthogneiss mylonite. **C)** Inclined elliptical poly-phase domains of garnet + biotite + muscovite + plagioclase in a retrogressed felsic granulite that are consistent with dextral shear strain. Note location of sample 04G-029B dated in Figs. 7B and 7E.

liations and gently SW-plunging stretching lineations (Fig. 2; Dumond et al., 2010). Minor sinistral shear zones occur as conjugates to the dextral zones and together define a NW-SE sub-horizontal finite shortening direction (Fig. 2D; Dumond et al., 2010). The adjacent GRsz is dominated by penetrative NE-striking, steeply NW-dipping foliations with gently SW-plunging stretching lineations that exhibit predominantly dextral strike-slip kinematics with a minor component of SW-over-NE thrust-sense displacement (Fig. 3; Dumond et al., 2010). The northwest side of the transect adjacent to the GRsz is locally characterized in several places by Neoarchean orthogneisses and felsic granulite that are unconformably overlain by paragneisses, quartzite, and felsic granulite (Martel et al., 2008; Bethune et al., 2013; #3–4 in Fig. 1C). New data in this contribution documents structures, petrology, *P-T* conditions, and monazite petrochronology associated with partial melting in the Grollier Lake area northwest of the GRsz (#1 in Fig. 1C, Figs. 4–6, Figs. 7A and D). These data fill an important gap between the Snowbird Lake and Beaverlodge domains northwest of the GRsz (#1 between #3–4 in Fig. 1C). New data are also presented for syn-kinematic monazite in the GRsz and compared with previously published data for syn-kinematic monazite in the Mary batholith (Figs. 7B–C and 7E–F).

3. Methods

Major and trace element analysis via electron microprobe of silicate phases and monazite was carried out at the University of Massachusetts-Amherst Geosciences Electron Microprobe/SEM Facility. High-resolution X-ray mapping of phases was carried out prior to analysis with a Cameca SX50 electron microprobe. Stage X-ray maps for garnet, orthopyroxene, and plagioclase were generated at 15 kV and 150 nA using a focused beam, 10 μm step size, and 50 ms dwell time. Beam raster X-ray maps for monazite were produced at 15 kV and 200 nA with a focused beam and

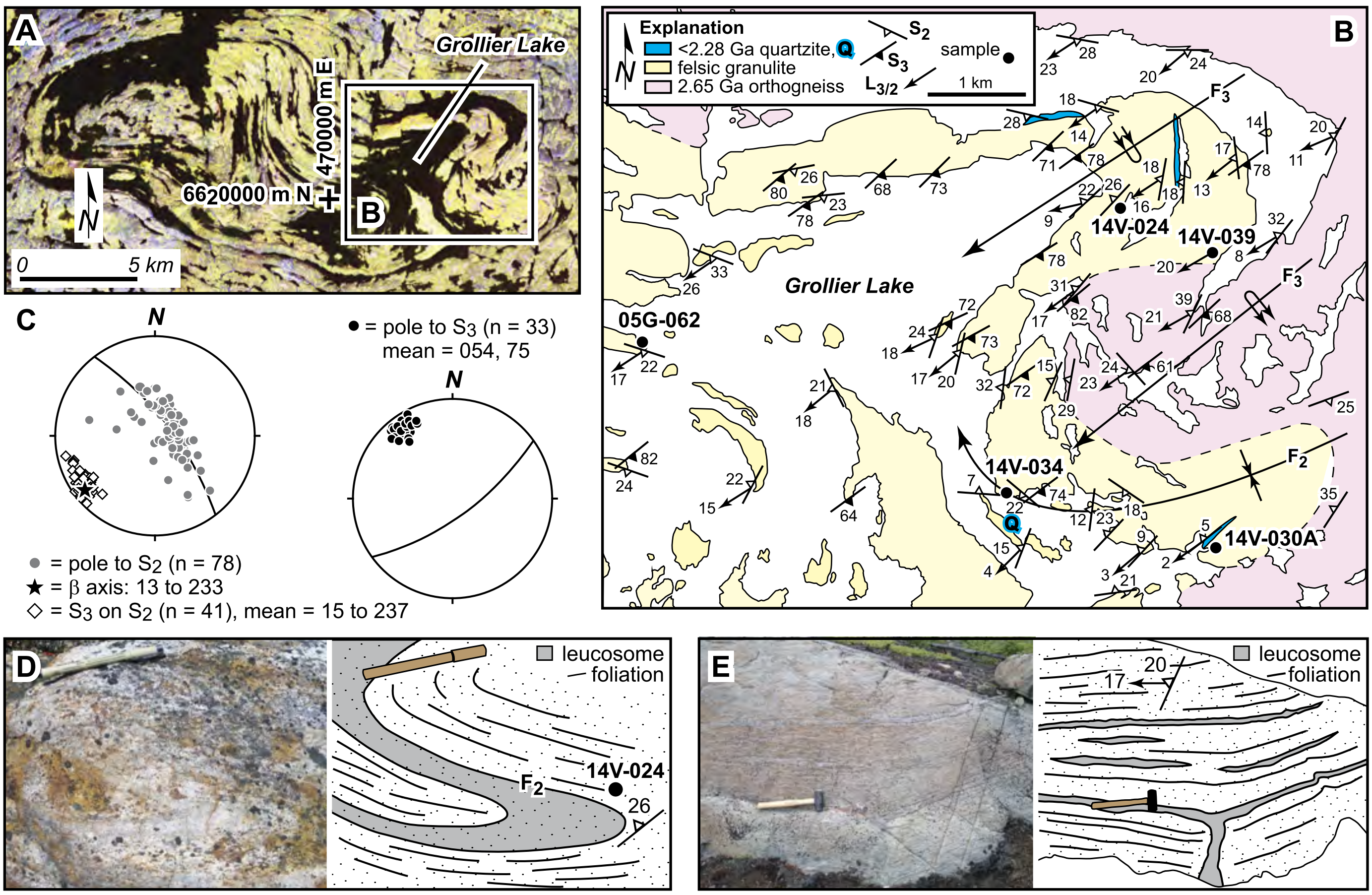

Fig. 4. Field observations and geologic map from the Grollier Lake region northwest of the Grease River shear zone, supplemented with data from Knox et al. (2011). **A)** ASTER satellite image indicating the location of the mapped area. Note that the water bodies (black) follow the gneissic fabric produced by a type 2 mushroom-crescent fold interference pattern. **B)** Geologic map of poly-deformed quartzite, felsic granulite, and basement orthogneiss. Recumbent F_2 folds and gently dipping gneissic fabrics are overprinted by overturned and gently SW-plunging F_3 folds with steeply SE-dipping cleavages. **C)** Stereonets summarizing structures in Fig. 4B. Both sets of fabrics are defined by leucosome. **D)** Early recumbent folds of garnet-bearing leucosome. Note location of sample 14V-024 dated in Figs. 7A and 7D. **E)** Outcrop illustrating the relationship between gently and steeply dipping leucosome-bearing fabrics in a deformed migmatite near Grollier Lake.

80 ms dwell time. Quantitative major element analyses of silicate phases, guided by the X-ray maps, were collected at 15 kV and 20 nA with a focused beam for garnet and orthopyroxene and a defocused beam (5 μm) for plagioclase and biotite (Table 1). Count times were 20 counts/s on peak and 10 counts/s on background. Calibrations were made using common natural and synthetic standards. Quantitative major and trace element analysis of monazite was carried out using the Cameca SX100 Ultrachron electron microprobe (Table S1). The Th-U-total Pb monazite dating analytical protocol is summarized in Williams et al. (2017), and the standards are described in Dumond et al. (2008). Electron probe microanalysis of monazite requires careful background analysis, particularly for Th, U, and Pb. This study utilized the new multipoint background approach of Allaz et al. (2019). Whole rock analysis of felsic granulite gneiss for use in phase equilibria modeling was obtained commercially via Activation Laboratories, Ltd. in Ancaster, Ontario, Canada.

4. Grollier Lake geology and *P-T* constraints northwest of the Grease River shear zone

The Grollier Lake area northwest of the Grease River shear zone is underlain by a heterogeneous suite of supracrustal rocks that lie unconformably upon a 2.65 Ga suite of granite, granodiorite, and quartz diorite orthogneisses (#1 in Fig. 1C; Figs. 4A–B; Knox et al., 2011; Ashton et al., 2017). Rocks above the unconformity consist of paragneisses that include variably migmatitic felsic granulites and <2.28 Ga quartzite interlayered with the granulites, supporting <2.28 Ga deposition of sedimentary protoliths upon exhumed Neoarchean basement (Fig. 4B; Knox et al., 2011; Ashton et al., 2017; this study). Early D_1 structures in the metasedimentary cover sequence include penetrative gently dipping foliations defined by garnet + leucosome folded into recumbent, tight to isoclinal F_2 folds in migmatitic felsic granulites (Figs. 4D and 5A–C). Gently dipping gneissic fabrics (S_2) defined by garnet ± orthopyroxene ± sillimanite and leucosome occur axial-planar the recumbent F_2 folds in the felsic granulites (Figs. 4C–E, 5D, and 6A). Overprinting D_3 structures include upright to overturned gently SW-plunging folds and intersection lineations associated with a steeply SE-dipping cleavage (S_3; Fig. 4B–C). Locally, the leucosomes parallel to S_2 can be traced continuously into the S_3 cleavage, suggesting that D_2 and D_3 may have been related to the same melting event (Fig. 4E). The intersection lineations also contain lineated K-feldspar ± garnet ± sillimanite. Superposition of D_2 and D_3 structures at the regional scale produced a 10s of km-scale type 2 mushroom-crescent fold interference pattern (Figs. 4A–B).

Pressure-Temperature (*P-T*) conditions northwest of the Grease River shear zone are well-constrained in the Snowbird Lake and Beaverlodge domains (#3–4 in Fig. 1C; Martel et al., 2008; Bethune et al., 2013). Few data, however, exist for a significant part of the Athabasca granulite terrane between the two locations (Fig. 1C). Granulites exposed in the Grollier Lake area thus provide a critical constraint in this region (#1 in Fig. 1C). The felsic granulites in the vicinity of Grollier Lake include Grt ± Opx + Pl + Kfs

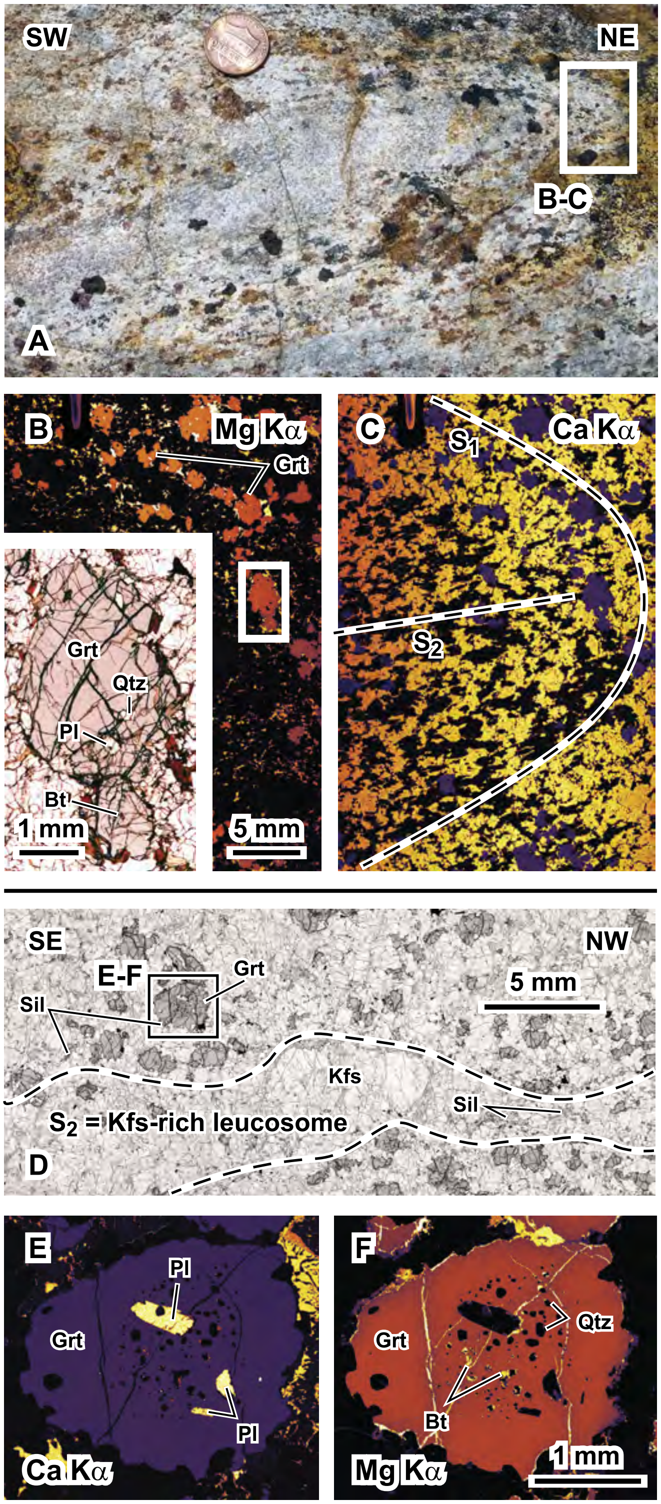

Fig. 5. Field and microstructural evidence for fluid-absent biotite melting and deformation of felsic granulites at Grollier Lake. **A)** Down-plunge field image of recumbent F_2 fold of garnet-rich leucosome. Penny for scale = 1.9 cm. **B–C)** Fold profile thin-section from outcrop (sample 14V-024 in Fig. 4B). **B)** Mg X-ray map illustrating S_1 defined by garnet (Grt). Inset is plane-polarized photomicrograph of peritectic garnet with inclusions of biotite (Bt) + plagioclase (Pl) + quartz (Qtz). **C)** Ca X-ray map illustrating folded garnet-rich layer (S_1) and penetrative S_2 cleavage defined by plagioclase + K-feldspar + quartz. **D)** Scanned thin-section of a garnet + sillimanite-bearing felsic granulite with S_2 defined by deformed K-feldspar-rich leucosome (sample 05G-062 in Fig. 4B). The section is perpendicular to the gently SW-plunging S_2 + S_3 intersection lineation at Grollier Lake. **E–F)** X-ray maps of peritectic garnet with inclusion-rich core containing inclusions of plagioclase + biotite + quartz.

± Sil + Bt + Qtz + Ilm assemblages with Zrn + Mnz ± Rt as accessory phases (Figs. 5 and 6A; mineral abbreviations after Bucher and Frey, 2002). Penetrative foliations (S_2 in Fig. 4B) and well-developed migmatitic layering are defined by Pl ± Kfs + Qtz-bearing leucosomes with porphyroblasts of Grt ± Opx (Figs. 5 and 6A). Orthopyroxene, up to 1 cm in diameter, is poikiloblastic with abundant euhedral inclusions of garnet up to 1.5 mm in diameter and less common inclusions of ilmenite (Fig. 6A). Orthopyroxene grains are unzoned and enriched in Al_2O_3 (5.39 wt.%; Table 1). Some Opx grains exhibit reaction rims up to 1 mm-wide due to replacement by anthophyllite (Fig. 6A). Garnet porphyroblasts up to 3 mm in diameter occur in the leucosome matrix and are typically inclusion-free (Fig. 6A) with some crystals containing inclusions of biotite, quartz, plagioclase, monazite, and/or zircon (Figs. 5B and E–F). Garnet grains exhibit flat zoning profiles ($Alm_{59}Prp_{35}Grs_5Sps_1$) with increases in Fe and decreases in Mg towards the rims and attributed to high-T diffusion during cooling (Fig. 6A; Table 1). Some garnet grains appear resorbed along their margins in contact with biotite and ilmenite. Observations of alteration of orthopyroxene rims to anthophyllite (Anh) and resorption of garnet to biotite are consistent with backreaction in the presence of melt (White and Powell, 2002). An alternative scenario for alteration of orthopyroxene would involve breakdown in the presence of fluid, e.g. Opx + H_2O → Anh. Taken together, the microstructural observations support growth of garnet, orthopyroxene, and K-feldspar during a fluid-absent biotite melting reaction of the type Bt + Pl + Qtz → Grt + Opx + Kfs + melt (sample 14V-039 in Fig. 6; Vielzeuf and Schmidt, 2001). For Opx-absent samples that contain Sil (e.g. Fig. 5D), a melting reaction of the type Bt + Pl + Sil + Qtz → Grt + Kfs + melt is permissible. Significant preservation of peritectic phases like Grt and Opx is consistent with the occurrence of melt loss (White and Powell, 2002).

P-T conditions were constrained with Perple_X 6.8.3 phase equilibria modeling in the NCKFMASHTO system using the whole rock bulk composition obtained for 14V-039 (Connolly, 2005; Na_2O + CaO + K_2O + FeO + MgO + Al_2O_3 + SiO_2 + H_2O + TiO_2 + Fe_2O_3; Table 1; Figs. 6B–D). The revised 2002 internally consistent thermodynamic database of Holland and Powell (1998) was used for the modeling (hp02ver.dat in Perple_X), along with the solution models listed in Table 2. The amount of H_2O used in the bulk composition for the modeling was constrained using a T-M(H_2O) diagram extending from 0–3 mol.% H_2O, a range that includes the bulk composition value for loss on ignition of 2.71 mol.% (0.75 wt.% in Table 1; Fig. 6B). The amount of H_2O at a pressure of 0.7 GPa was chosen to correspond with the lowest temperature at which orthopyroxene and garnet both occur on the solidus, coinciding with 2.71 mol.% H_2O (vertical arrow in Fig. 6B). The 0.7 GPa reference pressure was selected because it falls within the range of values estimated for felsic granulites in the Snowbird Lake and Beaverlodge domains, which like the Grollier Lake area, occur west of the Grease River shear zone (#3–4 in Fig. 1C; Martel et al., 2008; Bethune et al., 2013). Using the new bulk composition, ferric iron was adjusted using a T-X(Fe_2O_3) diagram (Fig. 6C). The amount of Fe_2O_3 was chosen to correspond to the minimum amount needed to stabilize the composition of orthopyroxene observed in 14V-039 within the peak assemblage stability field of Opx + Grt + Bt + Ilm + Qtz + Pl + melt (± Kfs) (vertical arrow in Fig. 6C). Larger values for Fe_2O_3 do not significantly impact the occurrence of Opx, but they do stabilize magnetite, which is not observed in the sample (Fig. 6C). The adjusted bulk composition was used to create a *P-T* phase equilibrium diagram with isopleths corresponding to the compositions for garnet and orthopyroxene in 14V-039 (Fig. 6D). Intersections of garnet isopleths coincide with the observed peak assemblage and occur at 875 °C and 0.7–0.8 GPa, and orthopyroxene Al_2O_3 compositions broadly overlap with these results (Fig. 6D). Models

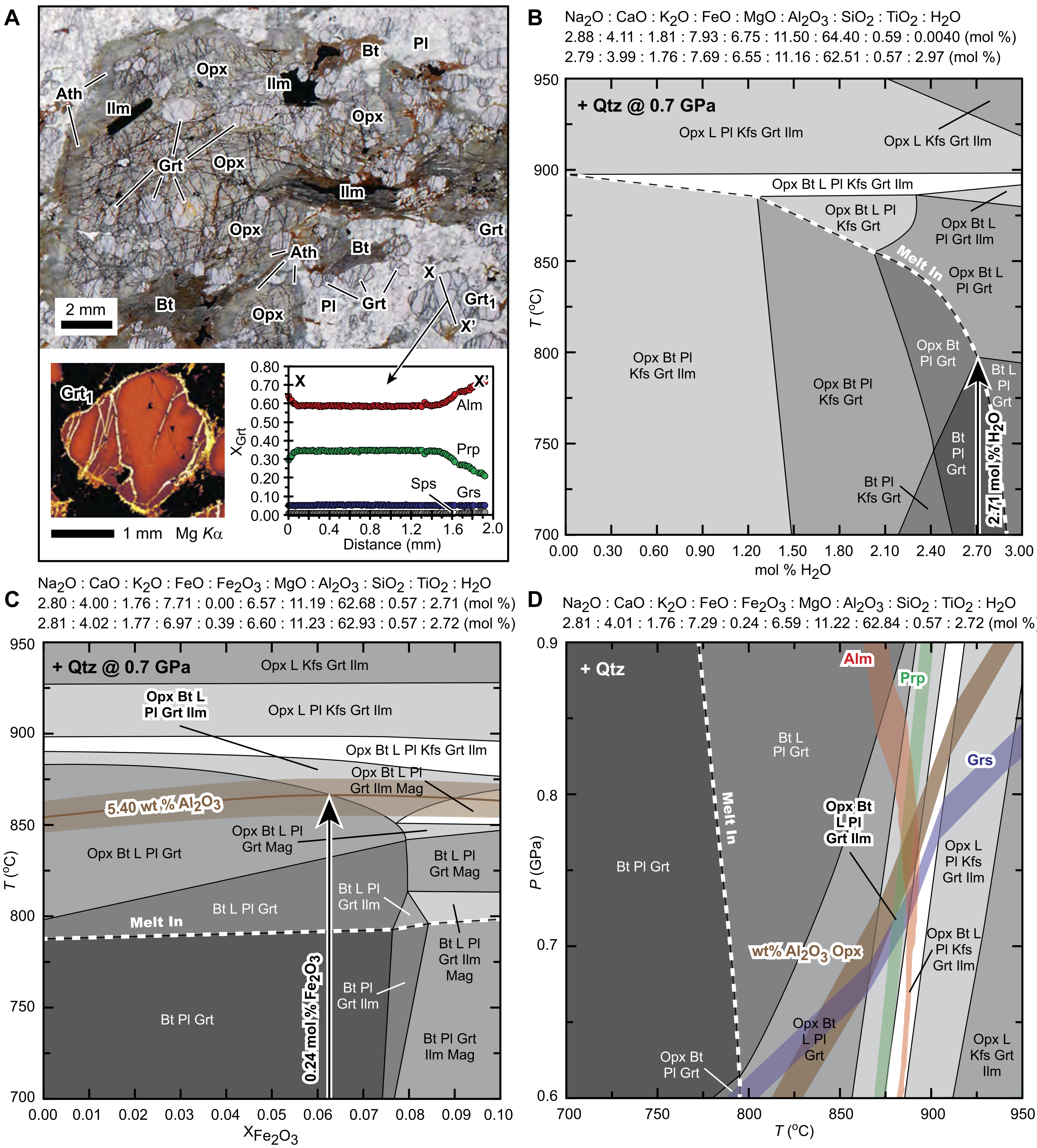

Fig. 6. Petrographic observations and phase equilibria modeling for sample 14V-039. Note location of sample in Fig. 4B. **A)** Plane-polarized photomicrograph of large poikiloblastic Opx grain with inclusions of Grt and Ilm. Magnesium X-ray map and electron microprobe profile indicate flat chemical zoning in Grt cores and diffusional modification of Fe and Mg across Grt rims. Opx = orthopyroxene; Grt = garnet; Ilm = ilmenite; Ath = anthophyllite; Bt = biotite; Pl = plagioclase; Alm = almandine; Prp = pyrope; Grs = grossular; Sps = spessartine. **B)** Temperature vs. M H_2O phase equilibria diagram exploring the impact of H_2O content on the bulk composition of 14V-039 at 0.7 GPa. The dashed white line in B–D indicates the solidus. The black arrow indicates the lowest temperature at which Opx + Grt occur on the solidus, located at 0.75 wt.% H_2O. **C)** Temperature vs. X Fe_2O_3 phase equilibria diagram exploring the effect of ferric Fe on the bulk composition at 0.7 GPa. The bulk composition at X Fe_2O_3 = 0 assumes all Fe is FeO (7.71 mol.%). For X Fe_2O_3 = 0.1, 10% of the bulk Fe is considered ferrous (0.39 mol.% Fe_2O_3). Note isopleth for wt.% Al_2O_3 in Opx for this sample. **D)** Phase equilibria diagram for *P-T* contoured with isopleths for Alm, Prp, and Grs in Grt and wt.% Al_2O_3 in Opx. Note intersections in the peak stability field of Opx + Grt + Pl + Ilm + Bt + Qtz + melt at 0.7–0.8 GPa and 875 °C.

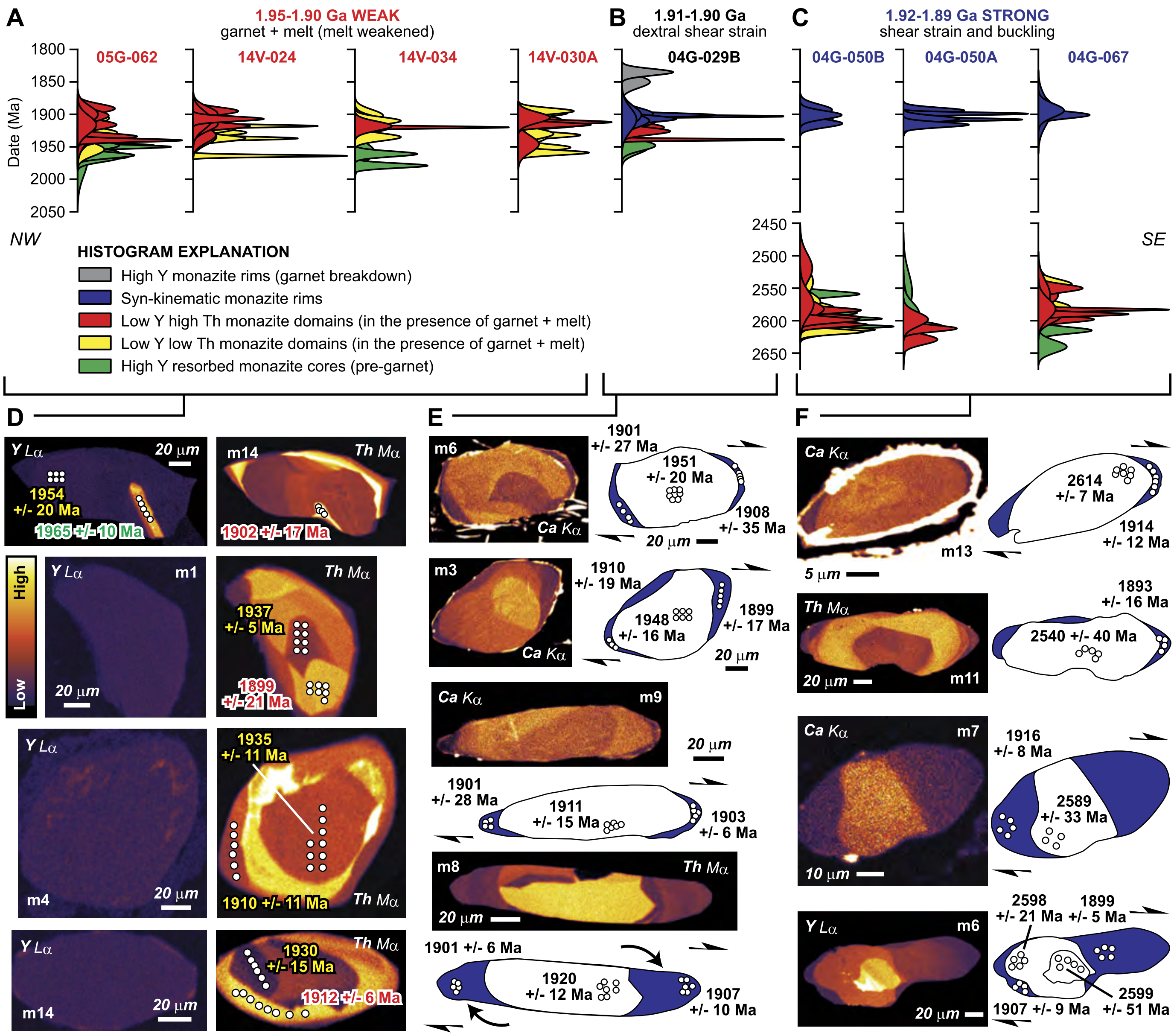

Fig. 7. Dating melt weakening and shear strain with monazite petrochronology applied to deep crustal felsic granulites. Dates in A–C are plotted as single Gaussian probability distributions for each analyzed domain, after Williams et al. (2006). **A)** Results from dating monazite in the Grollier Lake area northwest of the GRsz. **B)** Results from dating syn-kinematic monazite within the GRsz. **C)** Results from dating syn-kinematic monazite in the Mary batholith southeast of the GRsz (Dumond et al., 2010). **D)** X-ray maps and dates for monazite from Grollier Lake: samples from top to bottom = 05G-062, 14V-024, 14V-034, and 14V-030A. **E)** X-ray maps, dates, and sketches of dextral syn-kinematic monazite grains in 04G-029B from the GRsz. **F)** X-ray maps, dates, and sketches of dextral syn-kinematic monazite domains from a shear zone in the Mary batholith: top two grains from 04G-050B; bottom two grains from 04G-050A.

that explored variable amounts of H_2O and Fe_2O_3 did not significantly impact these *P-T* estimates. However, models with smaller amounts of H_2O stabilize orthopyroxene to unreasonably lower temperatures. Slightly higher pressures are predicted if no ferric iron is assumed.

The new data from Grollier Lake agree with *P-T* constraints gleaned from paragneiss felsic granulites exposed northwest of the GRsz in the Snowbird Lake and Beaverlodge domains (0.6–0.8 GPa and 760–850 °C as reported by Martel et al., 2008, and Bethune et al., 2013). Importantly, the new results from this study fill a crucial gap in data between the two domains (region #1 between regions #3 and #4 in Fig. 1C). These data are consistent with experimental constraints on fluid-absent melting of biotite-bearing metapelite and metagraywacke bulk compositions (Vielzeuf and Schmidt, 2001).

5. Dating melt weakening and shear strain in deep continental crust

Monazite petrochronology is focused on constraining the timing of major tectonic events, including metamorphism, melting, deformation, and fluid-mediated processes (Mahan et al., 2006; Yakymchuk and Brown, 2014, 2019; Dumond et al., 2015; Williams et al., 2017). Electron probe microanalysis and Th–U-total Pb dating, following the protocol of Williams et al. (2017) and Allaz et al. (2019), was applied to monazite in eight samples of peraluminous felsic granulite spanning the restored transect (A–A′ in Fig. 1C; Fig. 7; Table S1; Fig. S1). The goal was to determine if partial melting northwest of the GRsz in the Grollier Lake area and elsewhere was contemporaneous with dextral shear strain along the GRsz and in the Mary batholith southeast of the GRsz (regions #1–2 in Fig. 1C). Dates in this study range from 2.64–1.84 Ga with

Table 1
Silicate analyses and bulk composition.

Oxide (wt%)	Sample 14V-039[a]				
	Grt	Opx	Pl	Bt	Bulk
FeO	27.61	24.59	b.d.[b]	13.80	8.52
MgO	9.17	18.42	n.a.[c]	13.57	4.07
MnO	0.47	0.15	n.a.	0.01	0.10
CaO	2.03	0.18	8.42	b.d.	3.45
Na_2O	b.d.	0.02	6.86	0.12	2.67
K_2O	0.01	0.01	0.13	9.05	2.55
TiO_2	0.04	0.18	b.d.	3.12	0.70
Al_2O_3	22.30	5.39	26.57	17.32	17.54
SiO_2	39.19	49.76	58.38	37.80	57.90
P_2O_5	n.a.	n.a.	n.a.	n.a.	0.03
LOI[d]				0.75	
Total	100.84	98.71	100.35	94.78	99.24
Cations	Number of oxygens				
	12	6	8	11	
Fe	1.763	0.783	b.d.	0.855	
Mg	1.043	1.045	n.a.	1.498	
Mn	0.031	0.005	n.a.	0.001	
Ca	0.166	0.007	0.402	b.d.	
Na	b.d.	0.002	0.593	0.017	
K	0.001	0.001	0.008	0.855	
Ti	0.003	0.005	b.d.	0.174	
Al	2.006	0.242	1.396	1.511	
Si	2.991	1.894	2.602	2.799	
P	n.a.	n.a.	n.a.	n.a.	
End members					
Alm	0.587				
Prp	0.347				
Sps	0.0102				
Grs	0.0552				
En		0.570			
Fs		0.427			
An			0.40		
Ab			0.59		
Kfs			0.01		

[a] Location: UTM = 477097 m E, 6621965 m N Zone 13 V, NAD 1927.
[b] b.d. = below detection.
[c] n.a. = not analyzed.
[d] LOI = loss on ignition.

2-σ uncertainties on the order of 5–60 m.y. (Table S1). The magnitude of the uncertainties on these dates largely depend on X-ray counting statistics (and concentrations of Th, U, and Pb in each compositional domain), the degree of chemical homogeneity of the analyzed domain, uncertainty on background corrections, variations in conductive coating thickness, quality of calibration, and homogeneity of the calibration standards and consistency standard, among others (Williams et al., 2006). Results for the Moacir consistency standard from multiple analytical sessions carried out in this study are illustrated in Fig. S1.

5.1. Dating partial melting in the Grollier Lake area

For fertile metasedimentary rocks that experienced partial melting where garnet and monazite are the only Y-bearing phases, it can be common for monazite to exhibit resorbed high-Y cores mantled by low-Y domains that grew during or after crystallization of garnet which is a sink for Y (Bea and Montero, 1999). During melt crystallization, thorium partitions strongly into monazite (Xing et al., 2013), and low-Y Th-rich domains most likely represent crystallization from a peraluminous melt in equilibrium with peritectic garnet (Dumond et al., 2015). It is these Y-depleted Th-rich monazite domains that are thus critical for dating the occurrence of the peritectic reaction that produces garnet + melt and concurrent weakening in deep crustal felsic granulites.

Most monazite grains in the four Grollier Lake felsic granulite samples dated in this study display evidence for incomplete dissolution of high-Y cores. Dates for these resorbed cores range from 1.98–1.95 Ga and are considered pre-garnet growth (Figs. 7A and 7D). Low-Y monazite domains that mantle these cores consist of both low-Th and high-Th domains. Low-Y low-Th domains range from 1.96–1.90 Ga, and most likely grew during or after the appearance of garnet (Figs. 7A and 7D). Monazite inclusions in garnet that must have crystallized pre- to syn-garnet growth were dated at 1.97–1.90 Ga. Low-Y high-Th domains overgrowing high-Y cores or occurring as high-Th rims that must have crystallized in equilibrium with melt in the presence of garnet range from 1.95–1.90 Ga, a range that overlaps with dates for the low-Y low-Th domains (Figs. 7A and 7D). When combined with existing geochronology for felsic granulites from the Snowbird Lake and Beaverlodge domains (Martel et al., 2008; Bethune et al., 2013), the data reveal a 1000s of km^2 region of 1.95–1.90 Ga partial melting and deformation, as recorded in basement-cover sequences northwest of the Grease River shear zone (Fig. 1C).

5.2. Dating melting and dextral shear strain in the Grease River shear zone (GRsz) and the Mary batholith

Dates for Y-rich resorbed monazite cores in a retrogressed felsic granulite from the Grease River shear zone are 1.95 Ga (Figs. 7B and 7E). Y-depleted high-Th monazite cores and overgrowths indicate the occurrence of garnet + peraluminous melt by 1.94–1.91 Ga (Figs. 7B and 7E), and broadly contemporaneous with melting in the Grollier Lake area (Figs. 7A–B). For dating deformation in felsic granulite tectonites exposed in the GRsz, the goal was to identify syn-kinematic domains in monazite that exhibit σ- or δ-type asymmetric rims that constrain the timing of ductile shearing (e.g. Dumond et al., 2008). Several monazite grains in sample 04G-029B from the GRsz exhibit asymmetrically zoned rims defined by Ca and Th, consistent with dextral shear strain observed in outcrop (Figs. 3C and 7E). Many grains have σ-type zones defined by asymmetric overgrowths of Ca-poor rims on high-Ca cores (Fig. 7E). These rims are dated at 1.91–1.90 Ga (grains m3, m6, and m9 in Fig. 7E). Other grains with high-Th cores exhibit δ-type zoning defined by low-Th rims that are dated at 1.91–1.90 Ga (grain m8 in Fig. 7E). All syn-kinematic monazite rims in 04G-029B are Y-depleted and coincide with significant ThO_2 (8.51–16.98 wt.%: Table S1), supporting the inference that at least some component of 1.91–1.90 Ga ductile shearing was melt-present. Thin and rare high-Y rims occur on some grains and are attributed to growth during late-stage garnet breakdown in the presence of fluids at 1.85–1.84 Ga (Mahan et al., 2006; grey histograms in Fig. 7B). Dates for deformation in the 04G-029B felsic granulite are consistent with U-Pb zircon and Th-U-total Pb monazite dates for dextral shear strain recorded in a deformed leucogranite dike dated across strike of 04G-029B within the GRsz (Dumond et al., 2008).

In contrast to monazite from Grollier Lake and the GRsz, monazite grains in felsic granulites transposed into sub-horizontal fabrics within the Mary batholith record melting, resorption, and crystallization from melt in equilibrium with garnet at 2.60–2.55 Ga (Figs. 7C and 7F; Dumond et al., 2010). The felsic granulites locally occur in several steeply dipping 10s of m-scale dextral shear zones throughout the batholith with orientations that are sub-parallel to the GRsz (Figs. 2C–D; compare Figs. 2D and 3A). Monazite grains in these Archean felsic granulites exhibit syn-kinematic monazite domains defined by asymmetric low-Ca overgrowths dated at 1.92–1.89 Ga and similar to grains in the GRsz (compare Figs. 7B–C and 7E–F). The structural and geochronological data are consistent with buckling and dextral shear strain in the Mary batholith occurring contemporaneously with slip along the GRsz.

Table 2
Solution models used in Perple_X 6.8.3 phase equilibria models for 14V-039.

Phase	Model name	Independent end members	Source
Garnet	Gt(WPPH)	alm, py, gr	White et al. (2007)
Orthopyroxene	Opx(HP)	en, fs, mgts	White and Powell (2002)
Ternary feldspar	feldspar	abh, an, san	Fuhrman and Lindsley (1988)
Biotite	Bio(TCC)	tbit, east, ann, phl	Tajčmanová et al. (2009)
Ilmenite	Ilm(WPH)	oilm, dilm, geik	White et al. (2000)
Melt	melt(HP)	fo8L, fa8L, abL, anL, kspL, sil8L, h2oL	White et al. (2007)

6. Discussion

In combination with previously published results, data presented herein allows the reconstruction of a lower crustal rheological dichotomy across the Athabasca granulite terrane separated by the GRsz (Figs. 1C and 8A–B). New data from the Grollier Lake area demonstrate that high temperature (875 °C) deep crustal melt weakening (>25 km-depths = 0.7–0.8 GPa) occurred during dextral shear strain along the GRsz at 1.95–1.90 Ga. This contrasts with the record of Archean melting, dehydration, and subsequent isobaric cooling that occurred southeast of the GRsz, such that 1.92–1.89 Ga deformation was relatively non-penetrative and restricted to discrete 10s of m-scale shear zones and intervening folds (Dumond et al., 2010; this study). Importantly, the Mary batholith and adjoining domains east of the GRsz, at the latitude of Lake Athabasca, are interpreted to have experienced a protracted 650 m.y. period of lower crustal residence and cratonization between 2.55 and 1.9 Ga (residing at ∼0.9–1.1 GPa; Flowers et al., 2008; Dumond et al., 2010). Consequently, juxtaposition of the melt-weakened Grollier Lake area with the cratonic Mary batholith region represents a significant rheological dichotomy (Figs. 8A–B).

New and existing syn-kinematic monazite data from the GRsz and the Mary batholith demonstrate that dextral shear strain occurred at 1.92–1.89 Ga. Stretching lineations in both the 100s of km-scale GRsz and m-scale dextral shear zones in the Mary batholith are parallel and virtually coincident with the finite X-direction of strain determined in the Mary batholith for that interval of time (compare #2 and #3 in Fig. 8A; Dumond et al., 2010). Notably in the Grollier Lake area (#1 in Fig. 8A), intersection lineations defined by leucosome are also coaxial with this stretching direction and suggest that all three zones deformed contemporaneously during NW- to SE-directed sub-horizontal contraction in the Paleoproterozoic (Fig. 8A). New structural data from the Grollier Lake area presented in this study, combined with previously published mapping in the Mary batholith and the GRsz (Dumond et al., 2010), resemble a regional-scale positive flower structure that developed as a consequence of dextral transpressive shear strain (Fig. 8A). In this case, steeply SE-dipping leucosome-bearing cleavages in Grollier Lake are inclined towards the steeply NW-dipping fabrics in the GRsz and the Mary batholith (Fig. 8A). Outcrop- to regional-scale NE-trending upright to overturned folds occur on both sides of the GRsz, and are attributed to Paleoproterozoic transpressive strain reported throughout the Athabasca granulite terrane (Beaverlodge domain: Bethune et al., 2013; Grollier Lake: Knox et al., 2011, and this study; Snowbird Lake domain: Martel et al., 2008; Mary batholith: Dumond et al., 2010).

6.1. Tectonic setting for a deep crustal rheological dichotomy in the western Canadian Shield

Critical for understanding the Paleoproterozoic tectonic setting of the rheological dichotomy in the Athabasca granulite terrane is the timing of assembly of the Churchill province itself, in particular, the >2,000 km-long NE-trending Snowbird tectonic zone which separates the two cratonic domains that make up the Churchill province (Fig. 1A): the Rae and Hearne domains (Fig. 1C). At the latitude of Lake Athabasca, the Athabasca granulite terrane defines the eastern margin of the Rae domain juxtaposed against the Hearne domain along the >500 km-long Legs Lake thrust-sense shear zone with >20 km of vertical throw across the structure (Fig. 1C; Mahan and Williams, 2005; Mahan et al., 2006). Two main competing hypotheses for the Snowbird tectonic zone interpret the structure as (1) a circa 1.9 Ga suture between the Rae and Hearne domains (the Snowbird orogen of Hoffman, 1988, and Berman et al., 2007) or (2) a zone of 1.92–1.80 Ga intracontinental deformation affecting an already assembled Churchill province (Mahan and Williams, 2005; Dumond et al., 2008). The Athabasca granulite terrane is the most well-studied segment of the Snowbird tectonic zone (Dumond et al., 2018), and it includes the Snowbird Lake type-locality where it has been interpreted as a pre-1.92 Ga passive margin developed along the Rae domain (Martel et al., 2008; #3 in Fig. 1C). Both Neoarchean and Paleoproterozoic high-pressure granulites occur within the terrane (Fig. 1C), making it difficult to unequivocally attribute either suite of granulites to "old" or "young" assembly of the Churchill province.

Four crustal-scale shear zones divide the Athabasca granulite terrane into several lithotectonic domains. Two structures are extensional and facilitated exhumation of the terrane between 1.90 and 1.86 Ga: the Cora Lake shear zone (Regan et al., 2014) and the Wholdaia Lake shear zone (Thiessen et al., 2018). The third and largest structure, the 500 km-long Legs Lake shear zone, accommodated regional-scale thrust-sense 1.85 Ga uplift of the entire Athabasca granulite terrane and eastern Rae domain in its hanging wall over footwall rocks defined by the middle crustal (≤0.5 GPa) Hearne domain (Fig. 1C; Mahan et al., 2006). The geometry of this juxtaposition is similar to deep crustal uplifts worldwide, including the classic Kapuskasing Uplift in the Superior province (Percival et al., 1992). The fourth structure is the steeply NW-dipping Grease River shear zone which accommodated 1.92–1.80 Ga dextral transpressive strain, culminating with strike-slip offset of the entire terrane at 1.80 Ga (Mahan and Williams, 2005; Dumond et al., 2008). The setting for all four of the structures in their current geometry is most readily interpreted as intra-continental (Mahan and Williams, 2005). At the latitude of the Athabasca granulite terrane (59–60°N), no 1.9 Ga arc rocks have been identified along this central segment of the Snowbird tectonic zone that would support Paleoproterozoic subduction between the Rae and Hearne domains. Notably, none of the four major shear zones contain evidence that they accommodated suturing between the Rae and Hearne domains, such as ophiolite fragments or rocks of oceanic affinity. Furthermore, there is no evidence for closure of a Paleoproterozoic ocean between the Rae and Hearne domains at this latitude, apart from limited evidence for a Rae passive margin provided by Martel et al. (2008), the facing of which is unknown. Finally, at this same latitude, zircon U–Pb and Hf isotopic data from a suite of 2.60–2.55 Ga arc-related plutonic rocks that occur on both sides of the Legs Lake shear zone support the interpretation that the Rae and Hearne domains were assembled in the Archean (Regan et al., 2017). The model below thus favors an intracontinental setting for the Grease River shear zone.

During the 1.95–1.89 Ga interval of time documented in this study, Athabasca granulites were in the lower crust of the upper

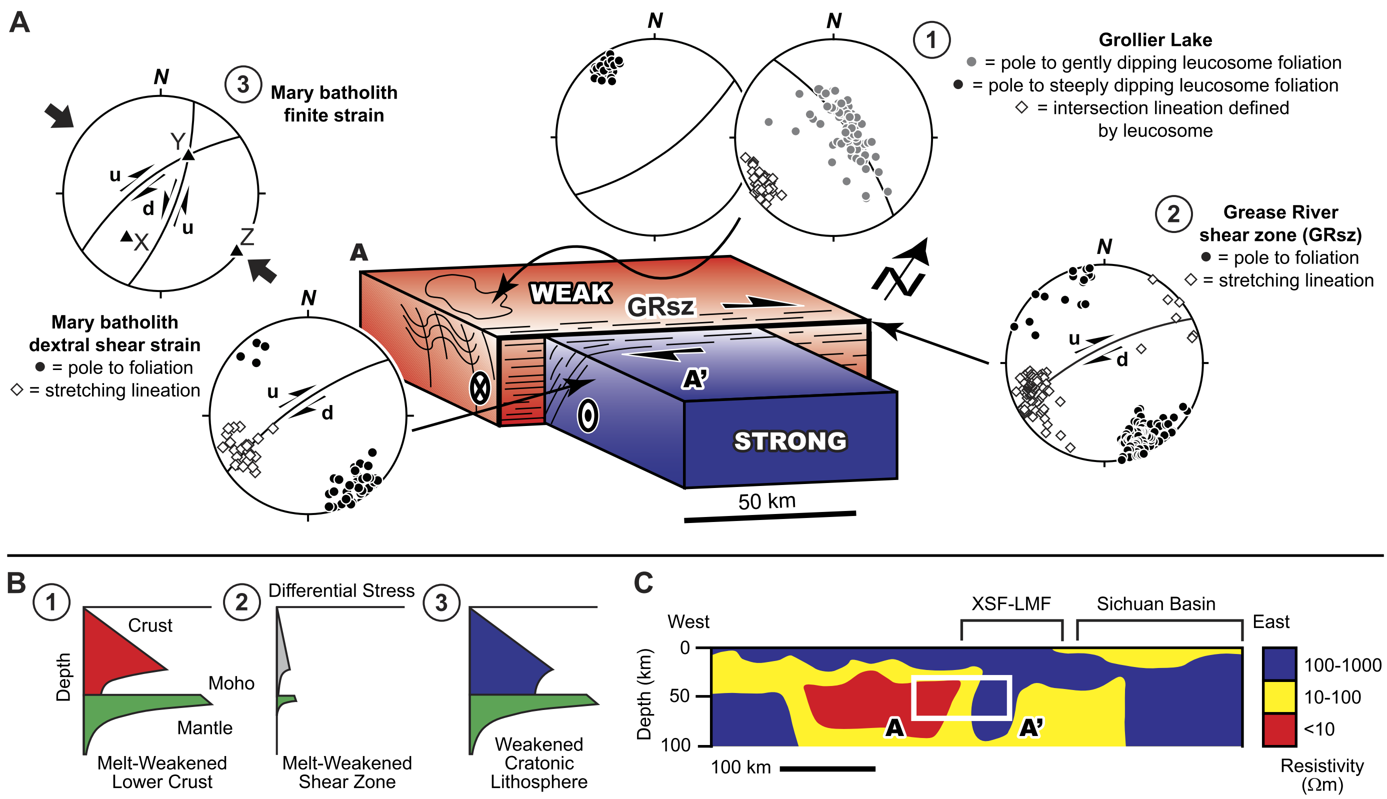

Fig. 8. **A)** Vertically exaggerated rheological block model with the strong Mary batholith domain in blue juxtaposed along the Grease River shear zone against the melt weakened Grollier Lake domain in red. Stereonets from the Grollier Lake area (#1) depict gently folded early S_1 and S_2 fabrics defined by leucosomes that are overprinted by a steeply SE-dipping cleavage that is locally defined by compositionally similar leucosomes. Intersection lineations between the fabrics are gently SW-plunging and sub-parallel to stretching lineations in the GRsz (#2). Stereonets for #3 illustrate the predominantly dextral steeply NW-dipping shear zones in the batholith that record predominantly strike-slip kinematics and a minor component of SW-over-NE thrust-sense during NW-to-SE sub-horizontal contraction (Dumond et al., 2010). These fabrics and kinematics are also similar to the Grease River shear zone (#2). **B)** Hypothetical qualitative strength profiles are illustrated for each region: #1 = melt weakened deep crust northwest of the GRsz; #2 = locally melt weakened GRsz; #3 = weakened cratonic lithosphere southeast of the GRsz. **C)** Simplified line drawing of magnetotelluric cross-section P3 that runs W-E across southeastern Tibet and the Sichuan basin from Bai et al. (2010). Red color is highly electrically conductive crust attributed to zones or channels of melt or elevated fluid content. Blue domains represent highly resistive crust, e.g. underlying the Sichuan basin. The white A–A′ rectangle is the zone interpreted to be analogous to Fig. 8A analyzed in this study from the Canadian Shield. XSF-LMF = Xianshuihe-Longmenshan fault zones.

plate Churchill province during protracted tectonism (Fig. 1A). Collision of the lower plate Slave province and lower plate Buffalo Head superterrane occurred during the Taltson-Thelon orogeny, in association with arc magmatism along the western margin of the Churchill province at 1.98–1.90 Ga (Fig. 1A; Card et al., 2014). Continental arc magmatism at 1.92–1.91 Ga occurred during NW-vergent subduction along the eastern margin of the Churchill province, represented by the Porter Bay complex in the southeastern Hearne domain (Maxeiner and Rayner, 2011; PB in Fig. 1A). Available and new geochronological data are thus consistent with the rheological dichotomy occurring during terrane collision along the western margin of the Churchill province and NW-directed subduction along its eastern margin (Fig. 1A). Below I explore the record of melting in felsic granulites in the Grollier Lake area and elsewhere northwest of the GRsz, the evidence for contemporaneous shearing along the GRsz and in the Mary batholith, and implications for the hypothesized rheological dichotomy across this region as an analogy for deep crust along the periphery of Tibet (Figs. 7, 8).

6.2. Monazite petrochronology and implications for a lower crustal rheological dichotomy

The occurrence of melt weakening is critical for viscosity reduction and flow in the deep crust of orogens (Beaumont et al., 2004). Deformation experiments on partially melted granite demonstrate that the onset of melting coincides with a significant drop in strength (at ∼7 vol.%: Rosenberg and Handy, 2005). Documenting this process in the rock record requires geochronometers like monazite that are sensitive to the presence of melt and peritectic phases like garnet in partially molten peraluminous rocks (Bea and Montero, 1999). Two decades of research on the monazite + melt system has demonstrated that monazite Y- and Th-zoning, in association with peritectic garnet, are some of the best tools for dating melt weakening in migmatites and felsic granulites during orogenesis (Bea and Montero, 1999; Yakymchuk and Brown, 2019). Y-depleted Th-rich monazite domains in leucosome and as inclusions in peritectic garnet represent accurate constraints on melt weakening because they date the fluid-absent melt reaction that produces garnet + melt. Limited studies have documented that monazite in metasedimentary granulites can grow along the supra-solidus (melt-present) segment of *P-T* paths in orogenic deep crust (Dumond et al., 2015; Yakymchuk and Brown, 2019). Most recently, Yakymchuk and Brown (2019) demonstrated that melt-present high-Th monazite grains and high-Th monazite rims can grow near the metamorphic peak during melt migration. Thorium partitions strongly into monazite when it crystallizes from melt (Xing et al., 2013), and low-Y high-Th domains of monazite dated at 1.95–1.90 Ga in this study are interpreted to have crystallized in the presence of melt + garnet (Figs. 7A–B and 7D–E). These dates constrain a component of melt weakening that overlaps with dates for dextral shear strain and melt weakening along the GRsz and coincident with discrete ductile deformation in the Mary batholith, within the resolution of the technique (Figs. 7A–C and 8A–B).

Weak lower crust in the Grollier Lake area (red strength profile #1 in Fig. 8B) contrasts with isobaric cooling of the Mary batholith following Neoarchean granulite-facies metamorphism southeast of the GRsz that resulted in strengthening (blue strength profile #3 in Fig. 8B). Subsequent deformation in the Mary batholith at 1.92–1.89 Ga was restricted to 10s of m-scale shear zones and intervening upright to overturned folds (Figs. 2, 7C, 7F, and 8A–B; Dumond et al., 2010). As discussed earlier, prior to 1.92–1.89 Ga, the lithosphere in the vicinity of the Mary batholith was likely cratonic (Flowers et al., 2008; Dumond et al., 2010). Reactivation of this cratonic lithosphere was most likely due in part to asthenospheric upwelling and re-heating via mantle-derived magmatism (Flowers et al., 2008; blue weakened cratonic strength profile #3 in Fig. 8B). Together, these data document the occurrence of a pronounced Paleoproterozoic lower crustal rheological dichotomy (Figs. 8A–B). Although certainly smaller in scale (compare Figs. 1A–B), the rheological dichotomy in the Athabasca granulite terrane may be analogous to lower crustal deformation along the margins of the Tibetan plateau (locations #1–3 in Fig. 1B).

6.3. Rheological dichotomies in Tibet

Magnetotelluric profiles throughout Tibet reveal several deep crustal zones of high conductivity inferred to represent melt-weakened channelized crustal flow within stronger domains of deep continental crust (Rippe and Unsworth, 2010; Le Pape et al., 2015). Alternatively, some of these conductive zones have been attributed to fluids and/or melts produced during prograde metamorphism along shear zone-fault systems (Bai et al., 2010; Zhang et al., 2015). Juxtaposition of rheologically different domains of deep crust has been inferred in both eastern and northern Tibet (#1–3 in Fig. 1B). Contrasting weak and strong rheological behavior has been inferred across the Kunlun fault near the Qaidam basin (#2 in Fig. 1B; Le Pape et al., 2015) and near the Altyn Tagh fault between the Qaidam and Tarim basins in northern Tibet (#3 in Fig. 1B; Zhang et al., 2015). In the Longmenshan region of eastern Tibet, this juxtaposition occurs adjacent to strong cratonic lithosphere beneath the Sichuan basin (#1 in Fig. 1B; Clark et al., 2005; Royden et al., 2008). Magnetotelluric profiles across the Longmenshan fault system support the occurrence of weak low viscosity flow of deep crust that is impeded by strong crust underlying the Sichuan basin (Fig. 8C; Bai et al., 2010; Zhao et al., 2012). This phenomenon appears strikingly similar to the Canadian Shield analog presented in this study, such that melt-weakened deep crust flowed coincident with shear strain along the edge of cratonic lithosphere (Figs. 8A and 8C). Results from this study demonstrate that Tibetan rheological dichotomies are permissible interpretations, and exhumed exposures of deep continental crust arguably provide important field-based analogs for this process.

6.4. Implications for Lower Continental Crust

This work supports the notion that the rheology of lower continental crust is spatially heterogeneous at <1 cm to 100s of km length-scales. Deep crust can also be temporally heterogeneous with weak domains becoming stronger due to dehydration and cooling, and strong domains becoming weaker during re-heating. Fertility, i.e. susceptibility to melting, also exerts an important control on lower crustal rheology. Melt weakening and flow during fluid-absent melting ($>750\,^{\circ}$C) and granulite-grade metamorphism is favored in "first-cycle" metasedimentary biotite-rich protoliths (as inferred for the Grollier Lake granulites in this study), though melt extraction will decrease this fertility (Yakymchuk and Brown, 2014). Older previously dehydrated and deformed polymetamorphic granulites, as in the Mary batholith and elsewhere southeast of the GRsz (Dumond et al., 2015), tend to be stronger and less prone to pervasive lower crustal flow. These older stronger lower crustal domains can become the locus for strain localization and juxtaposition with (melt) weakened domains, as inferred here for part of the Athabasca granulite terrane and the deep crust beneath the Longmenshan region of eastern Tibet (Figs. 8A and 8C). Consequently, lower crustal rheological dichotomies can have a profound influence on the distribution of intra-continental strain during orogeny and plateau development.

Declaration of competing interest

The authors declare that they have no known competing financial interests or personal relationships that could have appeared to influence the work reported in this paper.

Acknowledgements

Funding for this research was provided by U.S. National Science Foundation grant EAR-1255277. Remarks on the manuscript from reviewers Félix Gervais, Kevin H. Mahan, Renaud Soucy La Roche, Eric J. Thiessen, and Martyn J. Unsworth significantly improved the final presentation. Editor Rebecca Bendick is thanked for her guidance throughout the review process. Discussions with Christopher L. Andronicos, Philippe Goncalves, Sean P. Regan, and Michael L. Williams are greatly appreciated. Field assistance from Melissa V. Hornick, Christopher F. Kopf, Michael L. Williams, and Victoria R.L. Wood is gratefully acknowledged. Michael J. Jercinovic is thanked for outstanding assistance with microprobe analysis at the University of Massachusetts-Amherst. Stereonets were produced using Rod Holcombe's GEOrient software version 9.5.0.

Appendix A. Supplementary material

Supplementary material related to this article can be found online at https://doi.org/10.1016/j.epsl.2020.116375.

References

Allaz, J., Williams, M.L., Jercinovic, M.J., Goemann, K., Donovan, J., 2019. Multipoint background analysis: gaining precision and accuracy in microprobe trace element analysis. Microsc. Microanal., 1–17. https://doi.org/10.1017/S1431927618015660.

Andronicos, C.L., Velasco, A.A., Hurtado, J.M., 2007. Large-scale deformation in the India-Asia collision constrained by earthquakes and topography. Terra Nova 19, 105–119.

Ashton, K., Knox, B., Card, C., Rayner, N., Davis, B., Heaman, L., Creaser, R., 2017. Synthesis of U-Pb and Sm-Nd Geochronological Results from the Dodge Domain, Southeastern Rae Province, Volume 2: Summary of Investigations. Miscellaneous Report 2017-4.2, Paper A-12, Saskatchewan Geological Survey. 31 p.

Bai, D., Unsworth, M.J., Meju, M.A., Ma, X., Teng, J., Kong, X., Sun, Y., Sun, J., Wang, L., Jiang, C., Zhao, C., Xiao, P., Liu, M., 2010. Crustal deformation of the eastern Tibetan plateau revealed by magnetotelluric imaging. Nat. Geosci. 3, 358–362.

Bea, F., Montero, P., 1999. Behavior of accessory phases and redistribution of Zr, REE, Y, Th, and U during metamorphism and partial melting of metapelites in the lower crust: an example from the Kinzigite Formation of Ivrea-Verbano, NW Italy. Geochim. Cosmochim. Acta 63, 1133–1153.

Beaumont, C., Jamieson, R.A., Nguyen, M.H., Medvedev, S., 2004. Crustal channel flows, 1: numerical models with applications to the tectonics of the Himalayan-Tibetan orogen. J. Geophys. Res., Solid Earth 109, B06406. https://doi.org/10.1029/2003JB002809.

Berman, R.G., Davis, W.J., Pehrsson, S., 2007. Collisional Snowbird tectonic zone resurrected: growth of Laurentia during the 1.9 Ga accretionary phase of the Hudsonian orogeny. Geology 35, 911–914.

Bethune, K.M., Berman, R.G., Rayner, N., Ashton, K.E., 2013. Structural, petrological and U–Pb SHRIMP geochronological study of the western Beaverlodge domain: implications for crustal architecture, multi-stage orogenesis and the extent of the Taltson orogen in the SW Rae craton, Canadian Shield. Precambrian Res. 232, 89–118.

Bucher, K., Frey, M., 2002. Petrogenesis of Metamorphic Rocks. Springer, Berlin. 341 p.

Card, C.D., Bethune, K.M., Davis, W.J., Rayner, N., Ashton, K.E., 2014. The case for a distinct Taltson orogeny: evidence from northwest Saskatchewan, Canada. Precambrian Res. 255, 245–265.

Clark, M.K., Bush, J.W.M., Royden, L.H., 2005. Dynamic topography produced by lower crustal flow against rheological strength heterogeneities bordering the Tibetan Plateau. Geophys. J. Int. 162, 575–590.
Clark, M.K., Royden, L.H., 2000. Topographic ooze: building the eastern margin of Tibet by lower crustal flow. Geology 28, 703–706.
Connolly, J.A.D., 2005. Computation of phase equilibria by linear programming: a tool for geodynamic modeling and its application to subduction zone decarbonation. Earth Planet. Sci. Lett. 236, 524–541.
Copley, A., Avouac, J.-P., Wernicke, B., 2011. Evidence for mechanical coupling and strong Indian lower crust beneath southern Tibet. Nature 472, 79–81.
Dumond, G., Goncalves, P., Williams, M.L., Jercinovic, M.J., 2010. Subhorizontal fabric in exhumed continental lower crust and implications for lower crustal flow: Athabasca granulite terrane, western Canadian Shield. Tectonics 29, TC2006. https://doi.org/10.1029/2009TC002514.
Dumond, G., Goncalves, P., Williams, M.L., Jercinovic, M.J., 2015. Monazite as a monitor of melting, garnet growth and feldspar recrystallization in continental lower crust. J. Metamorph. Geol. 33, 735–762.
Dumond, G., McLean, N., Williams, M.L., Jercinovic, M.J., Bowring, S.A., 2008. High- resolution dating of granite petrogenesis and deformation in a lower crustal shear zone: Athabasca granulite terrane, western Canadian Shield. Chem. Geol. 254, 175–196.
Dumond, G., Williams, M.L., Regan, S.P., 2018. The Athabasca granulite terrane and evidence for dynamic behavior of lower continental crust. Annu. Rev. Earth Planet. Sci. 46, 353–386.
Fielding, E.J., McKenzie, D., 2012. Lithospheric flexure in the Sichuan Basin and Longmen Shan at the eastern edge of Tibet. Geophys. Res. Lett. 39, L09311. https://doi.org/10.1029/2012GL051680.
Flowers, R.M., Bowring, S., Mahan, K.H., Williams, M.L., 2008. Stabilization and reactivation of cratonic lithosphere from the lower crustal record in the western Canadian Shield. Contrib. Mineral. Petrol. 156, 529–549.
Fuhrman, M.L., Lindsley, D.H., 1988. Ternary-feldspar modeling and thermometry. Am. Mineral. 73, 201–215.
Hacker, B.R., Gnos, E., Ratschbacher, L., Grove, M., McWilliams, M., Sobolev, S.V., Wan, J., Zhenhan, W., 2000. Hot and dry deep crustal xenoliths from Tibet. Science 287, 2463–2466.
Hoffman, P.F., 1988. United Plates of America, the birth of a craton: Early Proterozoic assembly and growth of Laurentia. Annu. Rev. Earth Planet. Sci. 16, 543–603.
Holland, T.J.B., Powell, R., 1998. An internally consistent thermodynamic data set for phases of petrological interest. J. Metamorph. Geol. 16, 309–343.
Knox, B., Card, C.D., Ashton, K.E., 2011. Bedrock Geology of the Grollier Lake Area, Southeastern Dodge Domain (Parts of NTS 74P/11, /12, /13 and /14), Volume 2: Summary of Investigations. Saskatchewan Geological Survey, pp. 1–13.
Lease, R.O., Burbank, D.W., Zhang, H., Liu, J., Yuan, D., 2012. Cenozoic shortening budget for the northeastern edge of the Tibetan Plateau: is lower crustal flow necessary? Tectonics 31, TC3011. https://doi.org/10.1029/2011TC003066.
Le Pape, F., Jones, A.G., Unsworth, M.J., Vozar, J., Wei, W., Jin, S., Ye, G., Jing, J., Dong, H., Zhang, L., Xie, C., 2015. Constraints on the evolution of crustal flow beneath Northern Tibet. Geochem. Geophys. Geosyst. 16, 4237–4260.
Mahan, K.H., Goncalves, P., William, M.L., Jercinovic, M.J., 2006. Dating metamorphic reactions and fluid flow: application to exhumation of high-P granulites in a crustal-scale shear zone, western Canadian Shield. J. Metamorph. Geol. 24, 193–217.
Mahan, K.H., Williams, M.L., 2005. Reconstruction of a large deep-crustal terrane: implications for the Snowbird tectonic zone and early growth of Laurentia. Geology 33, 385–388.
Martel, E., van Breemen, O., Berman, R.G., Pehrsson, S., 2008. Geochronology and tectonometamorphic history of the Snowbird Lake area, Northwest Territories, Canada: new insights into the architecture and significance of the Snowbird tectonic zone. Precambrian Res. 161, 201–230.
Maxeiner, R., Rayner, N., 2011. Continental arc magmatism along the southeast Hearne Craton margin in Saskatchewan, Canada: comparison of the 1.92–1.91 Ga Porter Bay Complex and the 1.86–1.85 Ga Wathaman Batholith. Precambrian Res. 184, 93–120.
Percival, J.A., Fountain, D.M., Salisbury, M.H., 1992. Exposed crustal cross sections as windows on the lower crust. In: Fountain, D.M., Arculus, R., Kay, R.W. (Eds.), Continental Lower Crust: Developments in Geotectonics. Elsevier, Amsterdam, pp. 317–362.
Regan, S.P., Williams, M.L., Chiarenzelli, J.R., Grohn, L., Mahan, K.H., Gallagher, M., 2017. Isotopic evidence for Neoarchean continuity across the Snowbird Tectonic Zone, western Churchill Province, Canada. Precambrian Res. 300, 201–222.
Regan, S.P., Williams, M.L., Leslie, S., Mahan, K.H., Jercinovic, M.J., Holland, M.E., 2014. The Cora Lake shear zone, Athabasca granulite terrane, an intraplate response to far-field orogenic processes during the amalgamation of Laurentia. Can. J. Earth Sci. 51, 877–901.
Rippe, D., Unsworth, M., 2010. Quantifying crustal flow in Tibet with magnetotelluric data. Phys. Earth Planet. Inter. 179, 107–121.
Rosenberg, C.L., Handy, M.R., 2005. Experimental deformation of partially melted granite revisited: implications for the continental crust. J. Metamorph. Geol. 23, 19–28.
Ross, A.R., Brown, L.D., Pananont, P., Nelson, K.D., Klemperer, S., Haines, S., Zhao, W.J., Guo, J.R., 2004. Deep reflection surveying in central Tibet: lower-crustal layering and crustal flow. Geophys. J. Int. 156, 115–128.
Royden, L.H., Burchfiel, B.C., van der Hilst, R.D., 2008. The geological evolution of the Tibetan Plateau. Science 321, 1054–1058.
St-Onge, M.R., Searle, M.P., Wodicka, N., 2006. Trans-Hudson Orogen of North America and Himalaya-Karakoram-Tibetan Orogen of Asia: structural and thermal characteristics of the lower and upper plates. Tectonics 25, TC4006. https://doi.org/10.1029/2005TC001907.
Tajčmanová, L., Connolly, J.A.D., Cesare, B., 2009. A thermodynamic model for titanium and ferric iron solution in biotite. J. Metamorph. Geol. 27, 153–165.
Taylor, M., Yin, A., 2009. Active structures of the Himalayan-Tibetan orogen and their relationships to earthquake distribution, contemporary strain field, and Cenozoic volcanism. Geosphere 5, 199–214.
Thiessen, E.J., Gibson, H.D., Regis, D., Pehrsson, S.J., 2018. Deformation and extensional exhumation of 1.9 Ga high-pressure granulites along the Wholdaia Lake shear zone, south Rae craton, Northwest Territories, Canada. Lithosphere 10, 641–661.
Vielzeuf, D., Schmidt, M.W., 2001. Melting relations in hydrous systems revisited: application to metapelites, metagreywackes and metabasalts. Contrib. Mineral. Petrol. 141, 251–267.
White, R.W., Powell, R., 2002. Melt loss and the preservation of granulite facies mineral assemblages. J. Metamorph. Geol. 20, 621–632.
White, R.W., Powell, R., Holland, T.J.B., 2007. Progress relating to calculation of partial melting equilibria for metapelites and felsic gneisses. J. Metamorph. Geol. 25, 511–527.
White, R.W., Powell, R., Holland, T.J.B., Worley, B.A., 2000. The effect of TiO_2 and Fe_2O_3 on metapelitic assemblages at greenschist and amphibolite facies conditions: mineral equilibria calculations in the system K_2O-FeO-MgO-Al_2O_3-SiO_2-H_2O-TiO_2-Fe_2O_3. J. Metamorph. Geol. 18, 497–511.
Williams, M.L., Jercinovic, M.J., Goncalves, P., Mahan, K., 2006. Format and philosophy for collecting, compiling, and reporting microprobe monazite ages. Chem. Geol. 225, 1–15.
Williams, M.L., Jercinovic, M.J., Mahan, K.H., Dumond, G., 2017. Electron microprobe petrochronology. Rev. Mineral. Geochem. 83, 153–182.
Xing, L.B., Trail, D., Watson, E.B., 2013. Th and U partitioning between monazite and felsic melt. Chem. Geol. 358, 46–53.
Yakymchuk, C., Brown, M., 2014. Consequences of open-system melting in tectonics. Q. J. Geol. Soc. Lond. 171, 21–40.
Yakymchuk, C., Brown, M., 2019. Divergent behaviour of Th and U during anatexis: implications for the thermal evolution of orogenic crust. J. Metamorph. Geol. 37, 899–916.
Yao, H., van der Hilst, R.D., Montagner, J.-P., 2010. Heterogeneity and anisotropy of the lithosphere of SE Tibet from surface wave array tomography. J. Geophys. Res. 115, B12307. https://doi.org/10.1029/2009JB007142.
Zhang, L., Unsworth, M., Jin, S., Wei, W., Ye, G., Jones, A.G., Jing, J., Dong, H., Xie, C., Le Pape, F., Vozar, J., 2015. Structure of the Central Altyn Tagh Fault revealed by magnetotelluric data: new insights into the structure of the northern margin of the India-Asia collision. Earth Planet. Sci. Lett. 415, 67–79.
Zhao, G., Unsworth, M.J., Zhan, Y., Wang, L., Chen, X., Jones, A.G., Tang, J., Xiao, Q., Wang, J., Cai, J., Li, T., Wang, Y., Zhang, J., 2012. Crustal structure and rheology of the Longmenshan and Wenchuan Mw 7.9 earthquake epicentral area from magnetotelluric data. Geology 40, 1139–1142.